

See discussions, stats, and author profiles for this publication at: <https://www.researchgate.net/publication/306090269>

Variability of the Antarctic Coastal Current in the Amundsen Sea

Article in *Estuarine Coastal and Shelf Science* · August 2016

DOI: 10.1016/j.ecss.2016.08.004

CITATIONS

0

READS

104

7 authors, including:



Chang-Sin Kim

Korea Polar Research Institute

10 PUBLICATIONS 27 CITATIONS

[SEE PROFILE](#)



Kyoung-Ho Cho

Korea Polar Research Institute

18 PUBLICATIONS 64 CITATIONS

[SEE PROFILE](#)



Hyun-Cheol Kim

Korea Polar Research Institute

41 PUBLICATIONS 610 CITATIONS

[SEE PROFILE](#)



Jae Hak Lee

Korean Institute of Ocean Science and Techn...

53 PUBLICATIONS 634 CITATIONS

[SEE PROFILE](#)

Some of the authors of this publication are also working on these related projects:



Ecosystem Structure and Function of Marine Protected Area (MPA) in Antarctica [View project](#)

All content following this page was uploaded by [Chang-Sin Kim](#) on 21 September 2016.

The user has requested enhancement of the downloaded file. All in-text references [underlined in blue](#) are added to the original document and are linked to publications on ResearchGate, letting you access and read them immediately.



Variability of the Antarctic Coastal Current in the Amundsen Sea



Chang-Sin Kim^a, Tae-Wan Kim^{a,*}, Kyoung-Ho Cho^a, Ho Kyung Ha^b, SangHoon Lee^a,
Hyun-Cheol Kim^a, Jae-Hak Lee^c

^a Korea Polar Research Institute, Incheon, South Korea

^b Department of Ocean Sciences, Inha University, Incheon, South Korea

^c Korea Institute of Ocean Science and Technology, Ansan, South Korea

ARTICLE INFO

Article history:

Received 27 December 2015

Received in revised form

8 August 2016

Accepted 10 August 2016

Available online 11 August 2016

Keywords:

Antarctic Coastal Current (AACC)

Variability

Ekman vertical velocity

Dotson Ice Shelf

Amundsen Sea

ABSTRACT

The nature of the Antarctic Coastal Current (AACC) and its seasonal and non-seasonal (several-day) variability were investigated using long-term mooring data obtained near the Dotson Ice Shelf in the Amundsen Sea. The moored instruments were operated from February 2012 to January 2014 in the Dotson Trough, which is one of the deep troughs on the Amundsen Sea shelf. The hydrographic structure of sigma density distribution at the ice shelf (27.25 kg m^{-3} at the surface) was found to be higher than at the continental shelf (27.00 kg m^{-3}), whereas in the middle layer, 27.45 kg m^{-3} isopycnal extended to 300 m depth near the ice shelf but below 200 m depth in the offshore. The surface mixed layer thickened from the shelf break toward the ice shelf. This thickening was caused partially by coastal downwelling resulting from onshore Ekman transport and by Ekman pumping in the coastal area. The baroclinic component of the AACC near the Dotson Ice Shelf increased from July to October and decreased from January to June in 2013. In comparison with other potential driving forces, the seasonal and non-seasonal (short-term) variation of the AACC correlated well with density variability, determined principally by salinity variation. Therefore, it is suggested that the variability of the isopycnocline by Ekman pumping in the coastal area is one of the important factors controlling the seasonality and non-seasonal variability of the AACC.

© 2016 Elsevier Ltd. All rights reserved.

1. Introduction

The ice sheet around West Antarctica has experienced widespread loss over recent decades (Bindenschadler, 2006; Rignot et al., 2008; Dutrieux et al., 2014); a change that could contribute to global sea level rise (Scambos et al., 2004; Pritchard and Vaughan, 2007; Joughin et al., 2010). The Amundsen Sea is one region of West Antarctica that has changed most rapidly. Several studies have suggested that oceanic heat transport to the ice shelves by intrusion of warm Circumpolar Deep Water can contribute to the increase in basal melt rate (Walker et al., 2007; Jenkins et al., 2010; Wählin et al., 2010; Jacobs et al., 2011, 2012; Arneborg et al., 2012; Nakayama et al., 2013; Dutrieux et al., 2014; Ha et al., 2014).

The Antarctic Coastal Current (AACC; ACoC) is one of the interesting features of the Southern Ocean. Globally, it is the southernmost current, representing the subpolar regime, the entire

region south of the Antarctic Circumpolar Current and flows in a westward direction parallel with the Antarctic continent (Orsi et al., 1995; Whitworth et al., 1998; Mathiot et al., 2011). Sverdrup (1953) reported the first direct observations of the current along the Antarctic continental slope, which revealed a westward flow in the Weddell Sea. Whitworth et al. (1998) suggested the characteristics of the AACC change from a broad flow far from the coast to a narrow flow close to the coast. In the narrow continental shelf area, it is difficult to distinguish the locations of the AACC and Antarctic Slope Front (Heywood et al., 1998, 2004). The AACC is a fast and shallow flow in the continental shelf area and it is often associated with the front of the ice shelf (Jacobs, 1991; Heywood et al., 2004).

The strong westward flows of the AACC and Antarctic Shelf Front affect the dynamics of the ocean environment, such as the water masses and circulations in the area of the Antarctic continental shelf (Whitworth et al., 1998; Mathiot et al., 2011). Strong coastal currents flowing along the edge of the ice shelf increase the exchange of heat and mass at the seawater–ice shelf interface, accelerating the rate of ice shelf melt (Hellmer et al., 2012). Nakayama et al. (2014) established that the consequent dispersion

* Corresponding author.

E-mail address: twkim@kopri.re.kr (T.-W. Kim).

of ice shelf meltwater affects the ocean surface circulation and the formation of water masses. Their numerical simulations suggested that a slight increase in the rate of basal mass loss of the ice shelves of the Amundsen and Bellingshausen seas could substantially increase the transport of meltwater into the Ross Sea, by strengthening the melt-driven shelf circulation and westward coastal current.

The westward AACC is driven by wind stress and buoyancy forcing (Tchernia and Jeannin, 1980; Tchernia, 1981; Núñez-Riboni and Fahrbach, 2009; Combes and Matano, 2014). Núñez-Riboni and Fahrbach (2009) revealed four driving mechanisms that may potentially determine the seasonal variability of the AACC's barotropic and baroclinic components in the Weddell Sea. Wind-driven Ekman transport accounts for 58% of the total barotropic variation of the coastal current (Núñez-Riboni and Fahrbach, 2009), and the density gradient due to the presence of fresh and cool meltwater near the ice shelf between the Antarctic Surface Water (AASW) and Shelf Water represents its baroclinic component (Fahrbach et al., 1992). Ekman transport is related to wind stress, however, sea ice concentration affects the momentum transfer between the wind and the current by modifying the surface drag coefficient (Fennel and Johannessen, 1998; Lüpkes and Birnbaum, 2005).

The variability of the AACC in the Amundsen Sea is understood only superficially because of the relative dearth of measurements in this region. Moreover, the AACC in the Amundsen Sea advances in the non-slope region and it appears nearby the ice shelf. Quantifying the effect of each forcing on the variability of the AACC and on its barotropic and baroclinic components is necessary for fuller understanding of the dynamics of the AACC (Núñez-Riboni and Fahrbach, 2009). We undertook a summertime cruise in 2012 and 2014 onboard the icebreaker R/V *Araon* and obtained hydrographic data on a transect along the Dotson Trough, which included the Amundsen Sea polynya and sea ice region (Fig. 1). We also collated two years' data recorded by instruments moored near the Dotson Ice Shelf. Using these observational datasets, the objective of this study was to quantify the contributions of the driving mechanisms to the seasonality and non-seasonal (short-term) fluctuation of the coastal current in the Amundsen Sea. Specifically, we investigated the forces that contribute to the seasonal and non-seasonal variability of the AACC, and we considered how the hydrographic state affects the intensity of the AACC and what causes the hydrographic state to change.

This remainder of this paper is organized as follows. Section 2 describes information relevant to the observations and method used in the investigation. Section 3.1 describes the hydrographic condition of the westward AACC in austral summer and its long-term variation. Section 3.2 describes the seasonal variation of the AACC and its possible forcings. Section 3.3 describes the relationship between the AACC and non-seasonal variation of wind and density. Section 4.1 introduces a more specific description of the dynamics of the ocean circulation in the coastal area of Antarctica. Section 4.2 describes the weakening of the westward AACC by the baroclinic effect. Section 4.3 describes the relationship between the coastal current and Ekman pumping velocity. Our findings are summarized in Section 5.

2. Materials and methods

2.1. Data

Oceanic data were collected during hydrographic surveys and from moored stations (Fig. 1). Conductivity–temperature–depth (CTD) sensors (SeaBird Electronics 911+) were used to measure the background hydrographic structures (i.e., potential temperature and salinity), and the vertical profiles of current data were observed

using a 300-kHz lowered acoustic Doppler current profiler (LADCP; Teledyne RD Instruments).

The long-term data were collated by the moored stations from February 2012 to January 2014. To measure the temporal variability of potential temperature, salinity, and velocity, two moored stations were deployed in the study area (red circles in Fig. 1): K1 at the entrance of the continental shelf and K3 nearby the ice shelf. The water depths of K1 and K3 are about 525 m and 1057 m, respectively. The instruments deployed at these moored stations comprised of five recording current meters (RCM 11, accuracy: ± 0.15 cm/s) and four MicroCAT (SBE37 SM) instruments to measure temperature (accuracy: ± 0.002 K) and conductivity (accuracy: ± 0.0003 S/m). The RCMs were deployed at depths of 250 and 400 m at K1 and 220, 490, and 850 m at K3. The potential temperature and salinity observations were taken at depths of 250 and 400 m at K1 and 220 and 845 m at the K3 station. The LADCP data and long-term RCM data were processed using the same technique as Thurnherr (2010), and the water velocities were detided with the major 10 harmonic components using the barotropic tide model (Padman et al., 2002).

To identify the effects of atmospheric forcing and sea ice on the coastal current, wind and sea ice concentration (SIC) data were obtained from the European Centre for Medium-Range Weather Forecasts (ECMWF) ERA-Interim and the Special Sensor Microwave Imager/Sounder (SSMIS) of the Defense Meteorological Satellite Program (DMSP), respectively. Daily averages of the 6-hourly reanalysis wind data were determined for comparison with other daily variables (i.e., SIC). The horizontal grid resolution of the wind and SIC data were 0.25° and 3 km, respectively. We considered the isoline of 15% SIC as the division between the seasonal ice zone (SIZ) and a polynya. Fig. 1 shows the SIZ (interior area of the white hachured line) and the Amundsen Sea Polynya (un-hachured region; ice area in the south of the Amundsen Sea) averaged between January 12–16, 2012 (period of hydrographic observation). The direction of small white tick marks or hachures on the contour lines indicates greater SIC. To identify the effects of ocean stress, sea ice velocity data were taken from the Polar Pathfinder Daily 25 km EASE-Grid Sea Ice Motion Vectors Version 3 (Tschudi et al., 2016), which has horizontal resolution of 25 km.

In order to understand the dynamics of the AACC, we divided the baroclinic component from the current velocity, despite only having observations from three layers, using a similar method to Núñez-Riboni and Fahrbach (2009). The barotropic component was calculated as the vertical mean velocity of a spline-fitted vertical profile using the time series data from the three layers recorded by the moored stations. The baroclinic component for each level was considered by subtracting the barotropic component from each time series. Although this method for separating the barotropic component from the coastal current has some uncertainty, the calculated baroclinic component was sufficient to establish the cause of the seasonal variation of the AACC.

We conducted two analyses of the time series data to determine the seasonal and non-seasonal variations. To understand the seasonal cycle of the AACC, we subtracted the seasonal cycle of the local wind, SIC, wind stress curl, and moored hydrographic data using Butterworth low-pass filter lines with a cut-off period of 90 days, similar to Núñez-Riboni and Fahrbach (2009). To compare the short-term fluctuations, we calculated the time series of wind stress, density, and current velocity anomalies, which were subsequently reprocessed using the Butterworth band-pass filter with cut-off periods of between 7 and 90 days, to remove micro- and macro-scale (tides and seasonality) variations.

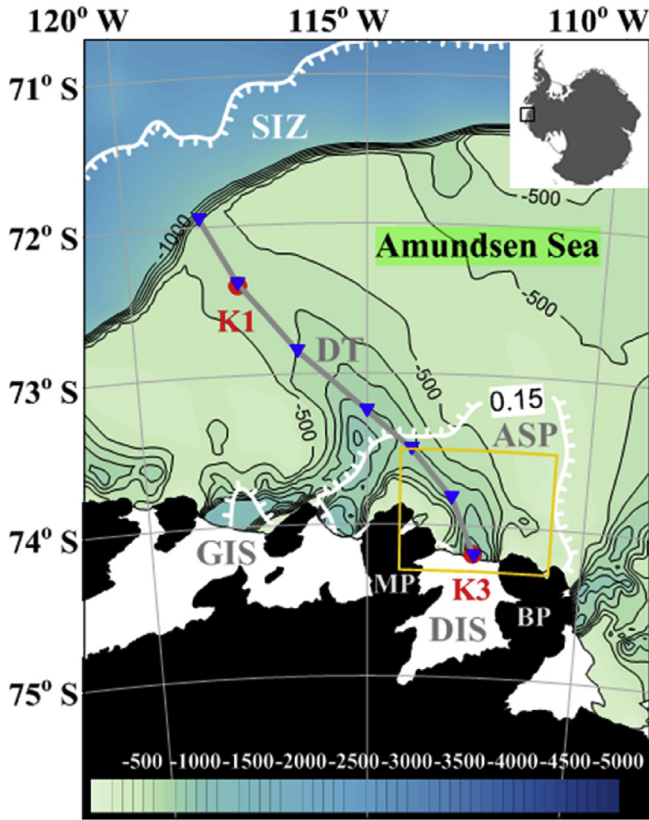


Fig. 1. Study area showing the CTD and moored stations. Red circles indicate the moored stations. Thick dashed line and inverted blue triangles indicate the section selected for the vertical hydrographic survey in the Dotson Trough during the R/V *Araon* expeditions. Labels: DIS – Dotson Ice Shelf, GIS – Getz Ice Shelf, MP – Martin Peninsula, and BP – Bear Peninsula. White hachured lines indicate uphill side of sea ice concentration and boundary of seasonal ice zone (SIZ) during the observation period of January 12–16, 2012 in the Dotson Trough and Amundsen Sea Polynya. Yellow rectangle indicates the area of the spatially averaged 10 m wind field. (For interpretation of the references to colour in this figure legend, the reader is referred to the web version of this article.)

2.2. Ocean surface stress and Ekman vertical velocity calculation

The ocean stress that acts on the surface of the ice-covered polar ocean is defined by both wind and ice motion. Under a homogeneous wind field, the difference between the ice–ocean and air–ocean drag coefficients generates the spatial variation of ocean surface stress at the ice margin (Häkkinen, 1986). In addition, the ice–ocean drag coefficient depends on sea ice properties such as roughness, length, thickness, and ice concentration (Lu et al., 2011). Therefore, the horizontal difference of ocean surface stress might increase or decrease depending on the upwelling (downwelling) at the ice margin (Häkkinen, 1986; Carmack and Chapman, 2003; Yang, 2006; Schulze and Pickart, 2012). Ekman transport and pumping are important factors for ocean general circulation and its variability. In particular, Ekman pumping drives basin-scale circulation in the subpolar oceans (Yang, 2006). Yang (2006) calculated the total stress forced by wind stress in open-water areas and established that surface momentum flux comes from both air–water and ice–water stresses in the ice-covered areas. Therefore, we used the following equation for ocean surface stress (τ_{ocn}):

$$\tau_{ocn} = (1 - A) \tau_{aw} + A \tau_{iw}, \quad (1)$$

where τ_{aw} is the ocean surface stress at the air–ocean boundary layer calculated by Large and Pond (1981), τ_{iw} is the ocean surface

stress at the ice–ocean boundary layer, and A is the SIC.

$$\tau_{aw} = \rho_a c_{aw} |\mathbf{U}_a| \mathbf{U}_a, \quad (2)$$

$$\tau_{iw} = \rho_w c_{iw} |\mathbf{U}_i - \mathbf{U}_w| (\mathbf{U}_i - \mathbf{U}_w). \quad (3)$$

In these equations, \mathbf{U}_a , \mathbf{U}_i , and \mathbf{U}_w are the velocity vectors of wind 10 m above the sea surface, ice, and seawater, respectively, ρ_a and ρ_w are the densities of air (1.29 kg m^{-3}) and seawater (1027 kg m^{-3}), respectively, and c_{aw} and c_{iw} are the air–ocean and ice–ocean drag coefficients, respectively, with approximate values of 1.6×10^{-3} and 4.5×10^{-3} , respectively (Koentopp et al., 2005). These drag coefficients were defined in the Weddell Sea but we used them in this study because of the dearth of data for the Amundsen Sea.

Ekman transport was calculated from the ocean surface stress as follows:

$$\mathbf{U}_E = \frac{1}{\rho_w f D_E} \tau_{y_ocn}, \quad \mathbf{V}_E = -\frac{1}{\rho_w f D_E} \tau_{x_ocn}, \quad (4)$$

where \mathbf{U}_E and \mathbf{V}_E are the zonal and meridional components of the Ekman transport, respectively, f is the Coriolis parameter, D_E is the depth of the Ekman layer with the 30 m, and τ_{x_ocn} and τ_{y_ocn} are ocean surface stresses calculated using Eq. (1).

The Ekman vertical velocity (\mathbf{W}_E) was calculated from the ocean surface stress as follows:

$$\mathbf{W}_E = \frac{1}{\rho_w f} \nabla \times \tau_{ocn}, \quad (5)$$

where f is the Coriolis parameter and $\nabla \times \tau_{ocn}$ is the curl of the ocean surface stress.

3. Results

3.1. Westward coastal current and hydrographic condition

Fig. 2a shows the horizontal baroclinic current distribution based on LADCP data, which reflects the vertically averaged ocean current of the upper 200 m in the ASP in 2012. A strong westward flow can be seen along the coastline near the Dotson Ice Shelf (southern part of the Amundsen Sea Polynya) and the maximum current velocity appears in front of the ice shelf where the westward flow is dominant. However, a dominant northwestward current flows along the isobaths to the north of the Martin Peninsula (MP; Fig. 1). The vertical profiles of the velocity components from the LADCP data indicate a strong westward upper-layer flow near the ice shelf (Fig. 2b). The zonal component of the coastal current is clearly distinguishable from the meridional component by its velocity magnitude. The maximum speed of the westward current exceeds 40 cm s^{-1} at 70 m depth and it decreases steadily with increasing depth.

The seawater in the Amundsen Sea is composed of three distinct water masses. A shallow halocline near the surface separates the fresher Antarctic Surface Water (AASW) from the colder and saltier Winter Water (WW), which in turn, is separated from the Circumpolar Deep Water by a broad thermocline near the bottom, especially on the eastern flank of the Dotson Trough (Assmann et al., 2013; Ha et al., 2014). Solar heating and meltwater input (i.e., glacial and sea-ice) generate a relatively warm and fresh water mass as the AASW in summer (Randall-Goodwin et al., 2015). During the cold season, WW is generated from surface cooling, which accompanies sea ice formation (Fahrbach et al., 1992). Fig. 3 shows the distributions of potential temperature, salinity, and

density along the Dotson Trough. The observed property of the potential temperature of the WW in the Amundsen Sea agrees with previous studies (<-1.6 °C; Bindoff et al., 2000; Wählin et al., 2010), and it remains preserved below the AASW until summer.

The surface mixed layer in the coastal area is thicker than in the region of the continental shelf break. In the surface mixed layer, between 73.2°S and 73.5°S, a relatively high temperature and an area of minimum salinity distribution was observed (Fig. 3a–b). Moreover, the surface salinity in the coastal area is higher than in the continental shelf region. The minimum-density water mass is distributed in the surface layer at 73.5°S, which is located at the northern boundary of the Amundsen Sea Polynya, as shown Fig. 1. This distinguishing feature of a minimum-density core (Fig. 3c) in the surface mixed layer appears to be related to the distribution of the SIZ (boundary of the polynya), which shows relatively lower salinity than the coastal area. Fig. 3d shows a potential temperature–salinity (θ – S) diagram of the Dotson Trough; the tendency shown in the diagram is comparable with Fig. 3 in Randall-Goodwin et al. (2015).

The density distribution corresponds well with the salinity distribution (Fig. 3b–c). From the surface down to 50 m depth, the density is relatively high near the ice shelf compared with the continental shelf. However, at the 200 m layer, lower density appears near the ice shelf. It increases slightly to the north and the 27.45 kg m⁻³ isopycnal rises from the Dotson Ice Shelf to the continental shelf. The vertical structure of density in the Dotson Trough is comparable with previous research on frontal structure (Sverdrup, 1953; Heywood et al., 1998). Heywood et al. (1998) investigated the vertical structure of the geostrophic velocity and found that strong baroclinicity of the coastal current existed at 600 m depth in the Weddell Sea. Similarly, the variability mechanism of the westward coastal current in front of Dotson Ice Shelf can be found from the spatial variation of the isopycnals along the trough perpendicular to the coastline. The possibility of the isopycnal variation appears could be considered as follows: the influence of meltwater increases the mixed-layer depth near the Dotson Ice Shelf, and the deepening of isopycnals by Ekman downwelling near the ice shelf.

Fig. 4a is a schematic of the moored instrument system deployed at K3 station. Fig. 4b–e shows the time series of the reanalysis wind and current vectors observed using RCM

instruments for the two studied years. Fig. 4f shows progressive vector diagrams of the current velocities in the three layers, indicating a persistent flow of the coastal current at K3. A southeasterly wind is dominant around the Dotson Ice Shelf during this period (yellow rectangle in Fig. 1). The currents in the near surface and middle layers show a northwestward flow that moved about 7470 and 3260 km, respectively, during the observation period of 692 days. The bottom layer flow moved 1320 km in a prevailing northward direction, except for a short period when it moved northwestward. In this study, only the zonal components were used because a strong AACC was observed along the Antarctic coast (in particular, in front of the ice shelves). Moreover, the current vectors show strong seasonal variation, especially in the near surface layer. Therefore, to investigate the seasonality of the coastal current and its driving forces, we focused on the near surface layer at 220 m.

3.2. Seasonal variation of the AACC

To understand the dynamics of the AACC, we quantified the effects of the local wind, SIC, wind stress curl (Sverdrup transport), and thermohaline forcing related to warming/cooling and ice melting/freezing on the seasonal variability of the AACC, as in Núñez-Riboni and Fahrbach (2009). Fig. 5 shows the time series of wind forcing, SIC, zonal current velocities, potential temperature, salinity, and density (thin gray solid lines) with their low-pass filter lines with a cut-off period of 90 days (thick black solid lines). In this study, strong AACC indicates westward flow and related to negative amplitude (negative is westward flow). These time series show that the seasonal cycle of the AACC of the Amundsen Sea is different from that of the Weddell Sea (Núñez-Riboni and Fahrbach, 2009). In particular, in 2013, the barotropic westward flow was a minimum (nearly zero) in June and a maximum (negative value) in October in the Amundsen Sea (Fig. 5e), whereas it was a minimum in December and a maximum in May in the Weddell Sea. The baroclinic westward flow increases in austral winter and early-spring (from July to October) and decreases in austral summer and autumn (from January to June), particularly in 2013 (Fig. 5f). Thus, the barotropic and baroclinic components of the AACC in the Amundsen Sea show similar annual phases (minimum in June and July and maximum in October and November) comparable with

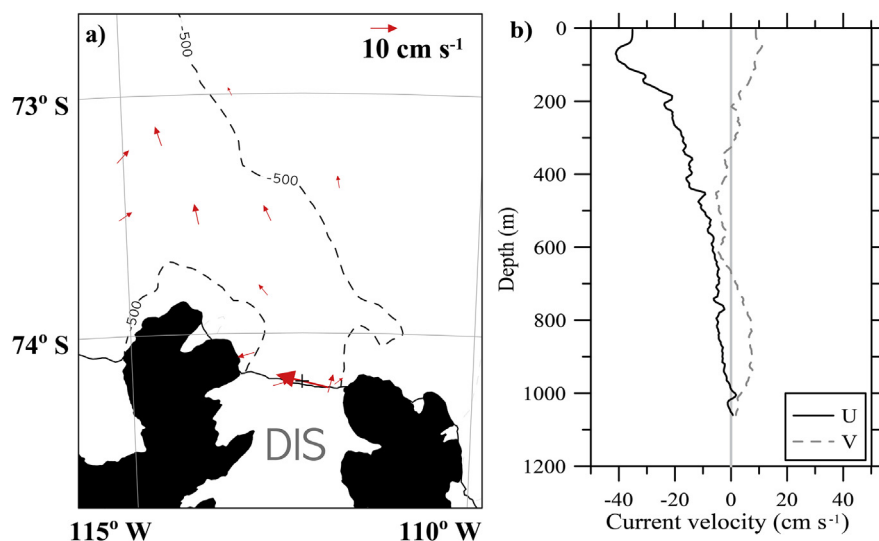


Fig. 2. a) Snapshot of baroclinic ocean surface current using LADCP data averaged over the upper 200 m in front of the Dotson Ice Shelf in 2012. b) Vertical profiles of current velocity (black cross in Fig. 2a) in front of the Dotson Trough.

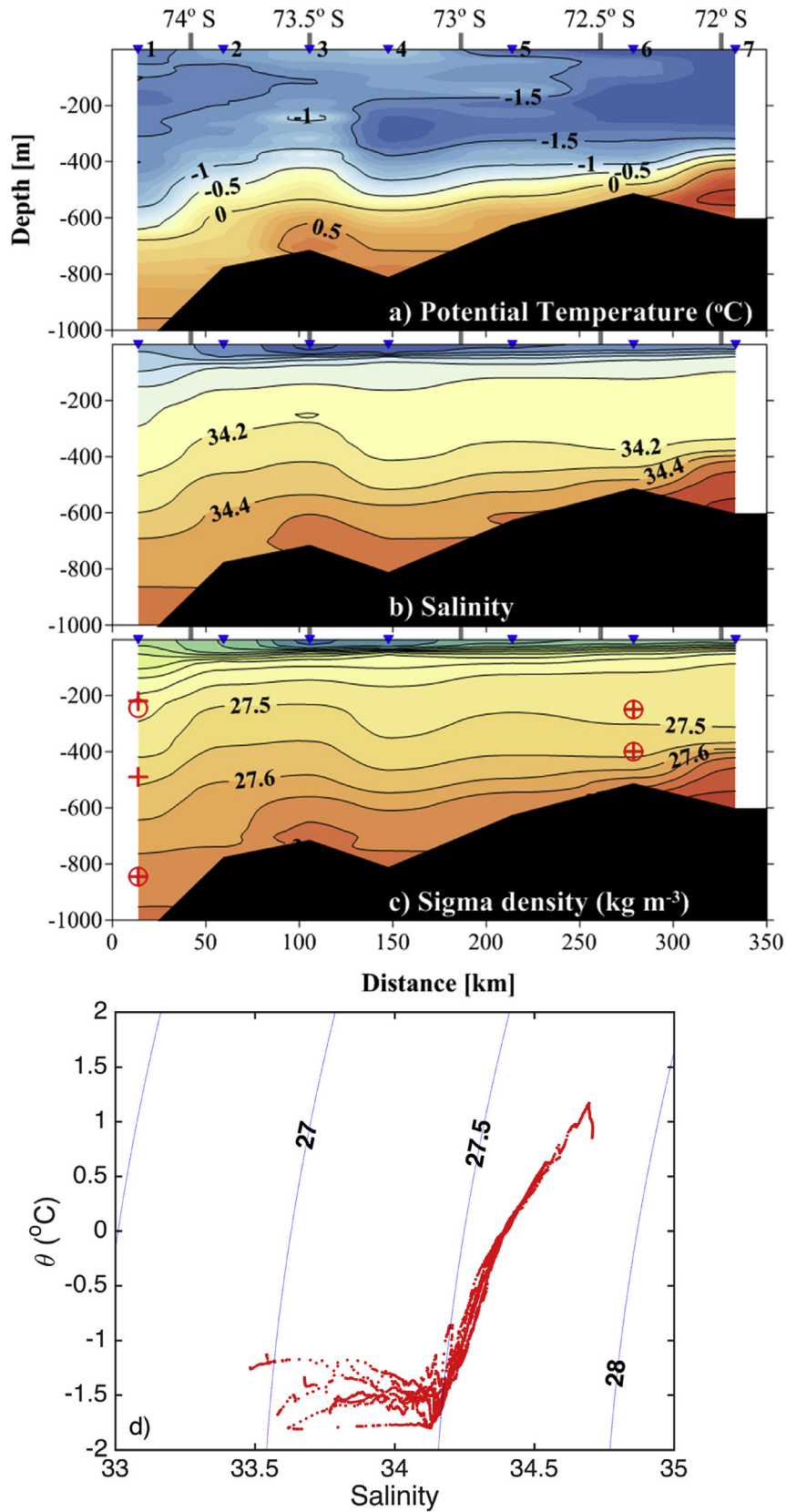


Fig. 3. Vertical section of a) potential temperature, b) salinity, and c) sigma density in the Dotson Trough. The x-axis and y-axis scales indicate the distance from the Dotson Ice Shelf to the continental shelf and water depth, respectively. Circles and cross symbols indicate long-term hydrographic and moored current meter positions. Bold gray ticks indicate latitudes per 0.5°. d) θ -S diagram for the Dotson Trough based on data from the 2012 cruise of the R/V *Araon*. The y-axis indicates the potential temperature.

studies of the Weddell Sea, but the maximum and minimum seasonal cycle is different. The SIC (Fig. 5d) and salinity (black line in Fig. 5g) in the near surface layer of K3 show distinct seasonal variations. However, no seasonal signals were detected from the local wind stress (Fig. 5a–b), suggesting that the direct effect of atmospheric forcing on the coastal current is relatively insignificant compared with the variability of salinity and density (Fig. 5i, k).

In order to understand the temporal variation of thermohaline forcing driven by the baroclinic pressure gradient, we compared the long-term density variations observed K3. Although we used the data observed between 245 and 845 m depths, the time series of the density variation showed distinct differences between the near surface and bottom layers near the ice shelf (Fig. 5g–l). Near surface sigma density variation (250 m) at K1 station from March 2012 to December 2013, no significant seasonal variation was found in the continental shelf region (not shown in here; mean = 27.497 kg m^{-3} , standard deviation = 0.014), whereas strong seasonal variation was shown near the ice shelf. The temporal variation of isopycnals (Fig. 5k) near the ice shelf was determined from the isohaline (Fig. 5i) than the isotherm (Fig. 5g). We suggest the possibility that seasonal variation of density near the ice shelf induces a horizontal baroclinic pressure gradient. Furthermore, such seasonal varying of baroclinic pressure gradient can lead to a variability of the coastal current.

The density distribution along the Dotson Trough in austral summer is determined mainly by salinity distribution (Fig. 3). Specifically, the sharp vertical density gradient between the surface and the depth of 200 m appears caused primarily by the vertical salinity gradient. In addition, the long-term observations of salinity,

temperature, and density at K3 indicate that near surface density variability (seasonal and non-seasonal) is highly dependent on salinity rather than on temperature variation (bold line in Fig. 5g, i).

Although the seasonality of the coastal current was slightly different from the variations of salinity and density, particularly in austral autumn 2012, most of the seasonality of the coastal current corresponded well with salinity and density. During the observation period, the baroclinic zonal current showed strong negative correlation ($R = -0.52$) with salinity variation, indicating that a strong/weak westward current coincides with a period of high/low salinity. Interestingly, this seasonal variability of salinity showed a phase difference with that of the SIC. During austral summer (February to March), near-surface salinity decreased despite the increasing of sea ice concentration, whereas salinity increased during austral winter (May to August). The phase difference between salinity and SIC suggested that the supply of freshwater by sea ice melting might be limited at sea surface.

The seasonal variation of salinity showed no significant correlation with temperature variability (Fig. 5g, i). Contrary to the temporal variation of temperature near-bottom, the amplitude of temperature variability near-surface was extremely small. Relatively small temporal fluctuation of temperature near surface suggests it is reasonable to suppose that seasonal variation of water density near the ice shelf is dependent on the vertical change of the mixed-layer depth induced by relative vertical motions of the water mass rather than changes of water mass by meltwater input from ice. Moreover, the fluctuation of salinity to depths of 400 m is larger than that of temperature in the well-conserved WW (Fig. 3). The vertical gradient of salinity is greater than that of temperature,

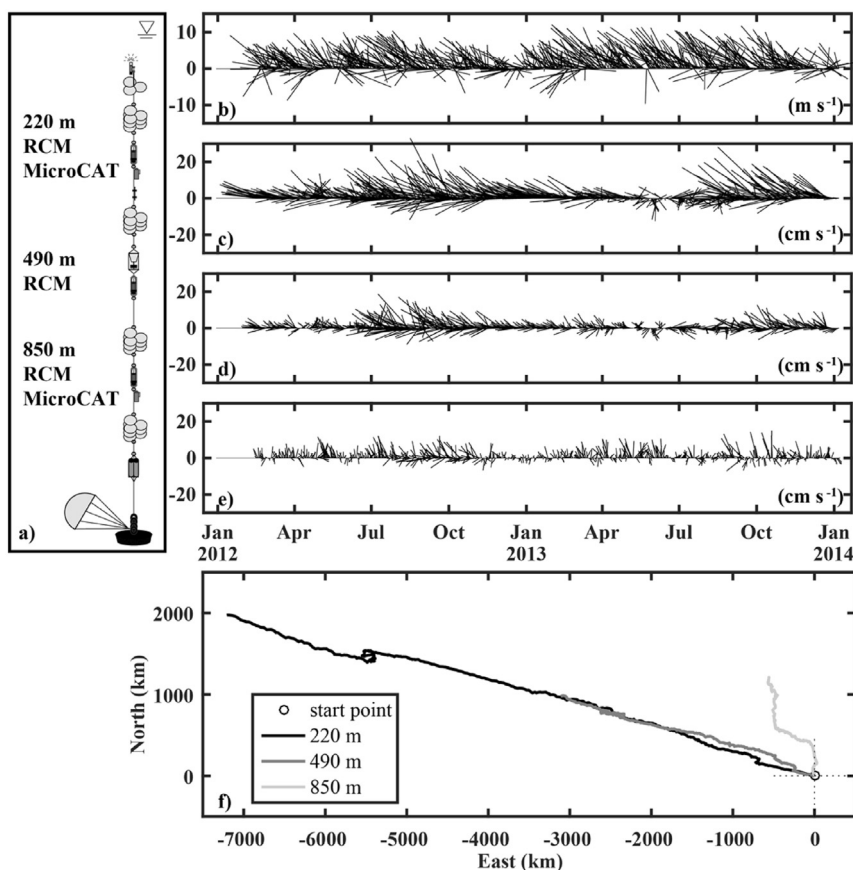


Fig. 4. a) Moored system at station K3 and time series of b) wind vectors on the Dotson Ice Shelf, current vectors in the c) near surface, d) middle, and e) bottom layers. f) Progressive vector diagrams of the three layers at K3. The x-axis and y-axis indicate the easting and northing distance, respectively, from mooring point.

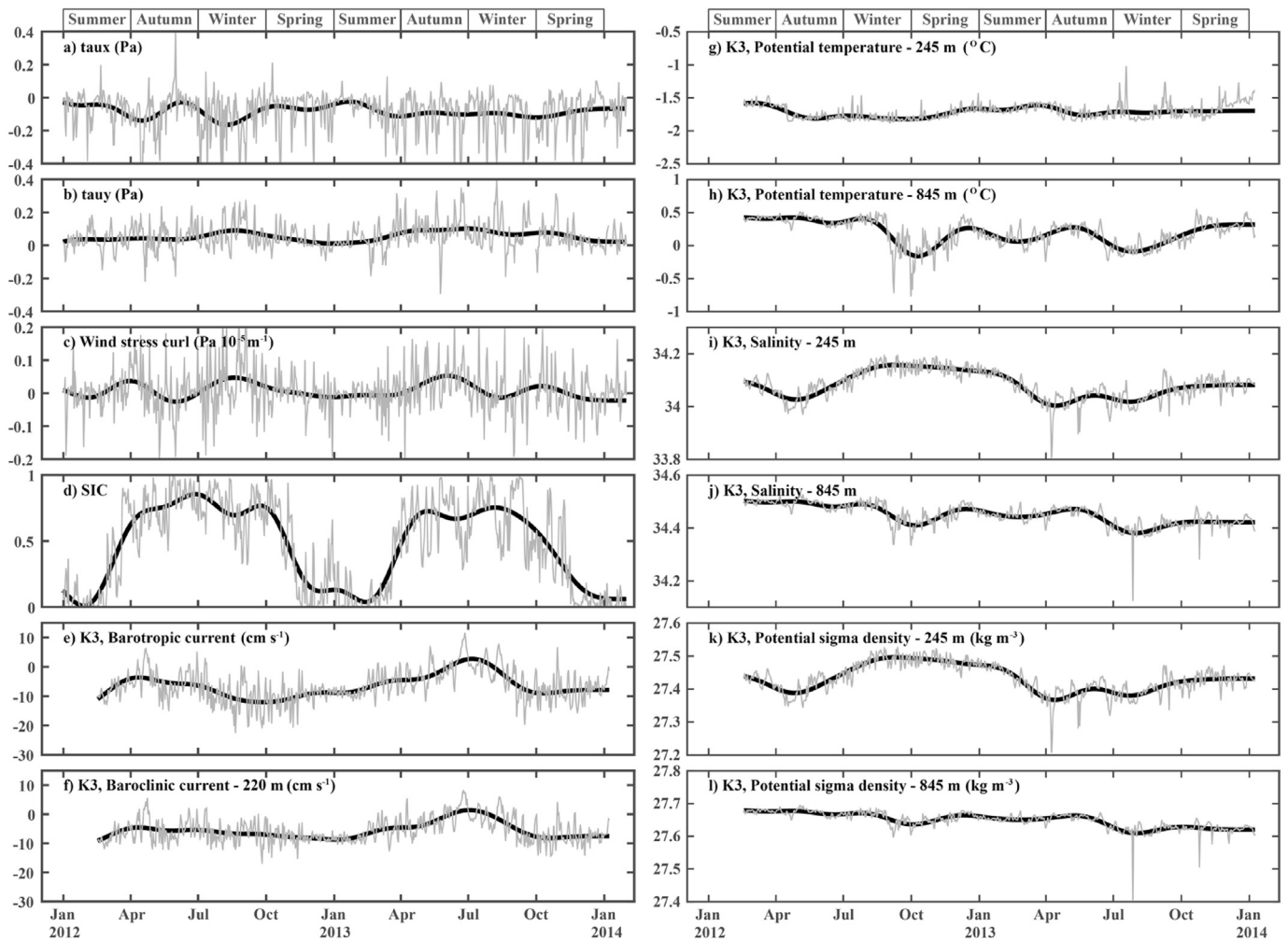


Fig. 5. Time series (thin gray solid lines) of a) and b) wind stress, c) wind stress curl, d) sea ice concentration (SIC), e) and f) zonal current velocity, g) and h) potential temperature, i) and j) salinity, and k) and l) potential sigma density near the Dotson Ice Shelf mooring station and their low-pass filter lines (thick black solid lines).

suggesting the possibility that it is caused by relative vertical motions of the water mass rather than by vertical mixing.

3.3. Non-seasonal variation

The water mass and circulation at the sea surface can change easily over periods shorter than seasonal time scales by changes of local wind patterns (Fahrbach et al., 1992). Moreover, atmospheric forcing shows strong short-term fluctuations, such as the increase/decrease of wind stress and positive/negative wind stress curl (Fig. 5a–c). To understand the details of the non-seasonal variability, we compared the time series of wind stress, density, and current velocity anomalies.

The upper-left panel in Fig. 6 presents time series of zonal wind speed and density anomalies. The time series of the zonal wind is based on spatial averaged values from near the Dotson Ice Shelf (yellow rectangle in Fig. 1). Positive/negative values indicate the anomaly of westerly/easterly winds. Fig. 6b illustrates the calculated cross correlation and lag analysis, which shows the strongest significant correlation of 0.26 between the zonal wind anomaly and the four-day lagged density anomaly. The maximum correlation in the positive domain implies the zonal wind anomaly coincides with the positive density anomaly (Fig. 6a). This positive correlation is presumably caused by coastal downwelling induced by the

southward Ekman transport related to the easterly wind. Coastal downwelling controls the decrease of near surface density in front of the ice shelf. As mentioned in Section 3.2, the baroclinic pressure gradient along the trough controls the variability of the westward coastal current. The lower panels of Fig. 6 show the relationship between the westward current and the density anomalies. It can be seen that the two variables are well matched (Fig. 6c) with a maximum significant correlation of 0.44 without time lag (Fig. 6d). Similar to the seasonal variation, the non-seasonal variability of the baroclinic coastal current corresponds well with the density variation. Thus, it can be considered that density change near the ice shelf is one of the important factors controlling the AACC in the Amundsen Sea.

4. Discussion

4.1. Dynamics

Fig. 7 is a schematic explaining the relationship between the baroclinic pressure gradient and the westward AACC in the coastal area. The easterly wind drives the southward Ekman transport toward the ice shelf, leading to an increase in the geopotential anomaly at the coast, which induces downwelling of the isopycnals (Heywood et al., 1998). This causes a mounding of the sea

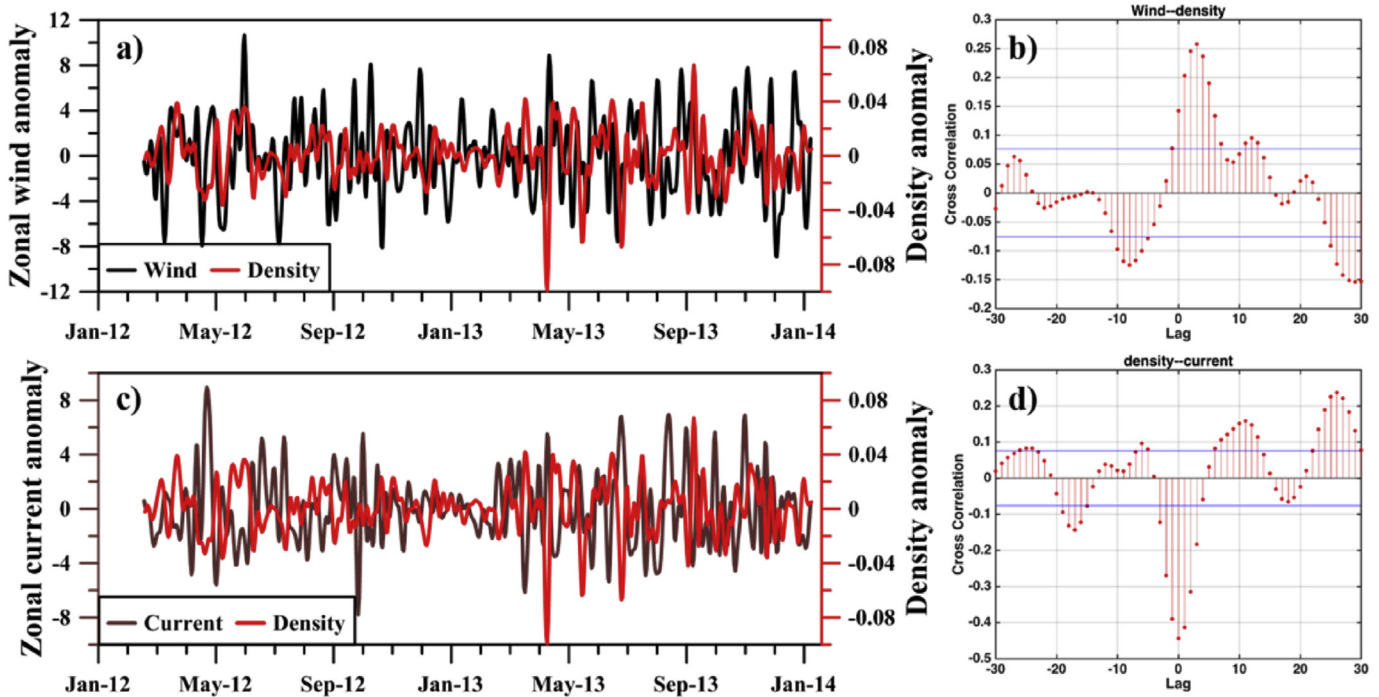


Fig. 6. Time series of wind, density, and current anomalies (left panels) and their time-lagged correlations (right panels). Blue lines in the right panels indicate 95% confidence intervals. (For interpretation of the references to colour in this figure legend, the reader is referred to the web version of this article.)

surface and a thickening of the pycnocline adjacent to the continent (Talley et al., 2011). The force associated with the seaward sea surface height (SSH) gradient induces a westward geostrophic flow, but the pycnocline (associated with the baroclinic pressure gradient) induces a negative (eastward) flow in the sub-surface layer, opposite to that of the AACC. This opposite flow weakens the westward flow near the ice shelf. If the easterly wind were stronger, it could be expected that the SSH gradient and downwelling would be enhanced, increasing the tilt of the isopycnals in the near surface layer. Variability of density in the near surface layer was strongly related with the salinity variation, which was found using austral summertime and long-term observations (Figs. 3 and 6a). Therefore, it was found that the westward flow and its weakening with depth associated with baroclinic effects

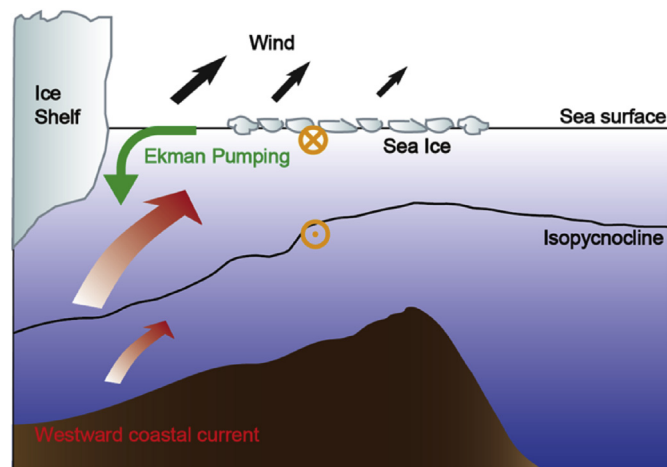


Fig. 7. Schematic of the relation between the easterly wind and current in the coastal area.

are caused by changes of isopycnals, suggesting thus density variation at the near surface is associated with thermohaline forcing mainly salinity variation. The variability of the AACC was coincident with hydrographic changes including seasonal and non-seasonal fluctuations.

4.2. Weakening of the coastal current

Summer hydrographic observations were used to quantitatively estimate the effects of the baroclinic pressure gradient along the Dotson Trough. Although, data from K1 and K3 can be used to estimate the seasonality of the baroclinic pressure gradient, uncertainty remains because of the large distance between the two mooring points and limitations in the observed layer of temperature and salinity. In order to further understand weakening the coastal current, we calculated the cumulated vertical velocity using Eq. (5) at the two CTD stations near the ice shelf (CTD 1 and 2; reversed diamonds in Fig. 3a), which clearly distinguishes the features between the two points. The nearest hydrographic station (CTD1) from the ice shelf showed downwelling at about 177 m about a year, whereas secondary station (CTD2) showed upwelling at about 74 m at the same time. Ekman vertical velocity difference appears to change the coastal current.

Additionally, we calculated the baroclinic pressure gradient along the Dotson Trough using the two CTD observations closest to the Dotson Ice Shelf to estimate the baroclinic effect on the weakening of the westward current. Although hydrographic data are limited in the summer, they are considered sufficient for identifying the baroclinic effect. The weakening of the westward current by the baroclinic effect was calculated using the momentum balance between the Coriolis force and the baroclinic pressure gradient according to

$$\mathbf{u}^* = \frac{g}{f \rho_w} \int_{-z}^0 \frac{\partial \rho}{\partial y} dz, \quad (6)$$

where \mathbf{u}^* is the current velocity associated with the baroclinic effect.

In the summer observation period, the westward current was weakened (ca. 1 cm s^{-1}) by the baroclinic effect up to a depth of 220 m (reference with the long-term mooring depth). In autumn and winter, the low-density area near the Dotson Ice Shelf could exacerbate the weakening of the westward current further by increasing the baroclinic pressure gradient.

4.3. Ekman pumping

Ekman transport in the Amundsen Sea Polynya, caused primarily by the southeasterly wind (Figs. 4b and 8), increases toward

the ice shelf. The wind stress curl is negative in most areas of the Amundsen Sea, whereas it is positive near the Dotson Ice Shelf and to the south of Amundsen Sea Polynya (Fig. 8e). The strong southwestward Ekman transport and positive wind stress curl lead to the elevation of the SSH and to downwelling in coastal areas. However, the spatial and temporal variations of the sea ice distribution are important in evaluating the effect of local wind on the ocean surface dynamics in Polar Regions. During austral summer, strong northward katabatic winds and solar radiation form polynyas near the coastal region. The sea ice conditions of the polynyas, marginal ice zone, and ice zone influence the spatial variation of surface stress and clearly affect the ocean surface stress. Therefore, seasonal variation of sea ice conditions influences the seasonality of the Ekman vertical velocity (pumping/suction) under the relatively constant wind speed in the Southern Ocean, especially in the SIz.

The spatial and temporal variations of wind stress, ocean

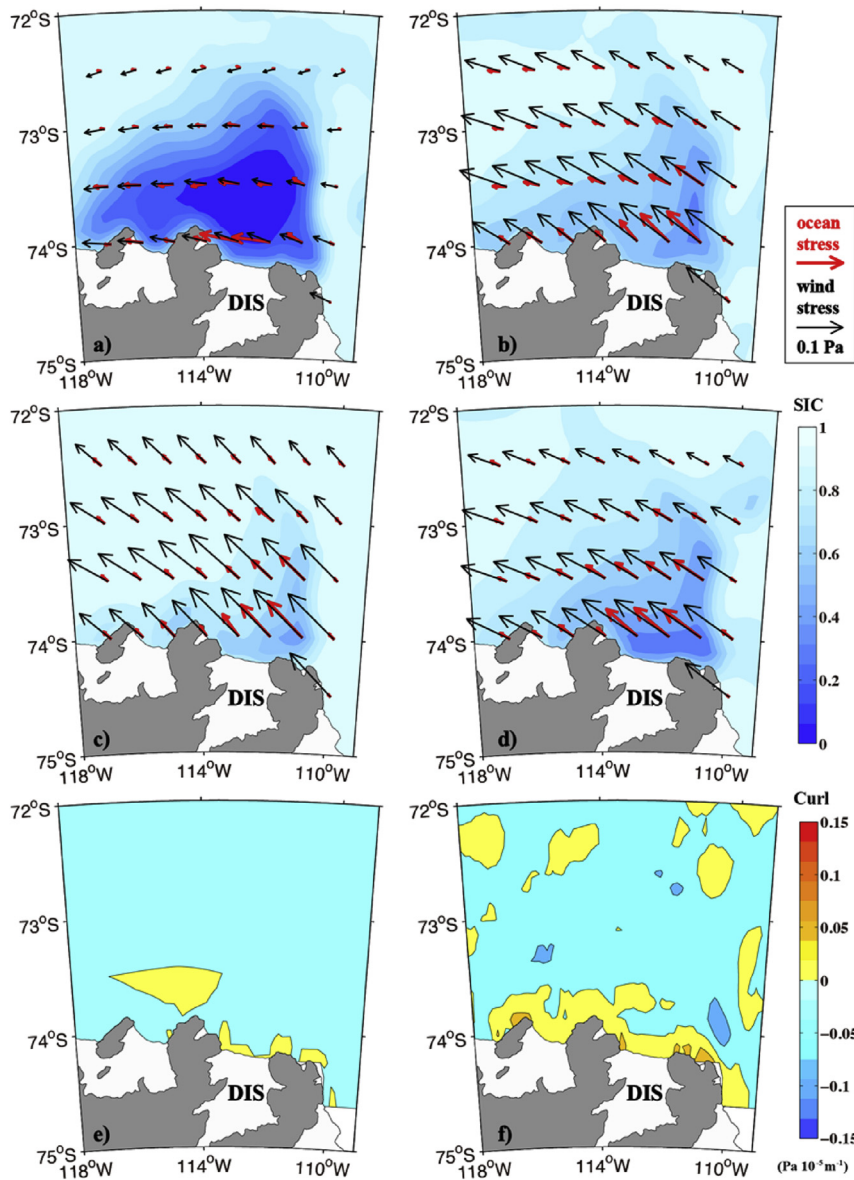


Fig. 8. Seasonally averaged ocean surface stress (red arrows), wind stress (black arrows), and sea ice concentration in a) austral summer (Dec 2013 to Feb 2014), b) autumn (Mar–May 2014), c) winter (Jun–Aug 2014), and spring (Sep–Nov 2014). Comparison of e) wind stress curl and f) ocean stress curl in summer. (For interpretation of the references to colour in this figure legend, the reader is referred to the web version of this article.)

surface stress (Eq. (1)), wind stress curl, ocean stress curl (Eq. (5)), and SIC are compared in Fig. 8. The ocean surface stress and wind stress are distinguished in the sea ice zone. The ocean stress curl is higher than the wind stress curl near the Dotson Ice Shelf (Fig. 8e, f), and the strength and direction of the ocean surface stress could be caused Ekman dynamics near the Dotson Ice Shelf. In order to understand the relationship between the changes in the coastal current and pycnocline in the coastal area, we compared the Ekman vertical velocity and coastal current. Fig. 9a represents the spatial correlation between the monthly averaged coastal current and Ekman vertical velocity calculated using Eq. (5), which considers the sea ice condition. High correlation with the westward coastal current can be seen in front of the Dotson Ice Shelf and the point of maximum correlation (circle) is located slightly to the northeast of the mooring point (cross). We calculated cross-correlation and lag analyses that showed the maximum significant correlation between the zonal wind anomaly and the four-day lagged baroclinic component of the coastal current (time lag of maximum correlation from Fig. 6b). The monthly averaged Ekman vertical velocity shows that downwelling during the observation period, which includes the strength of the Ekman vertical velocity, leads to the variability of the coastal current (Fig. 9b). The time series of the

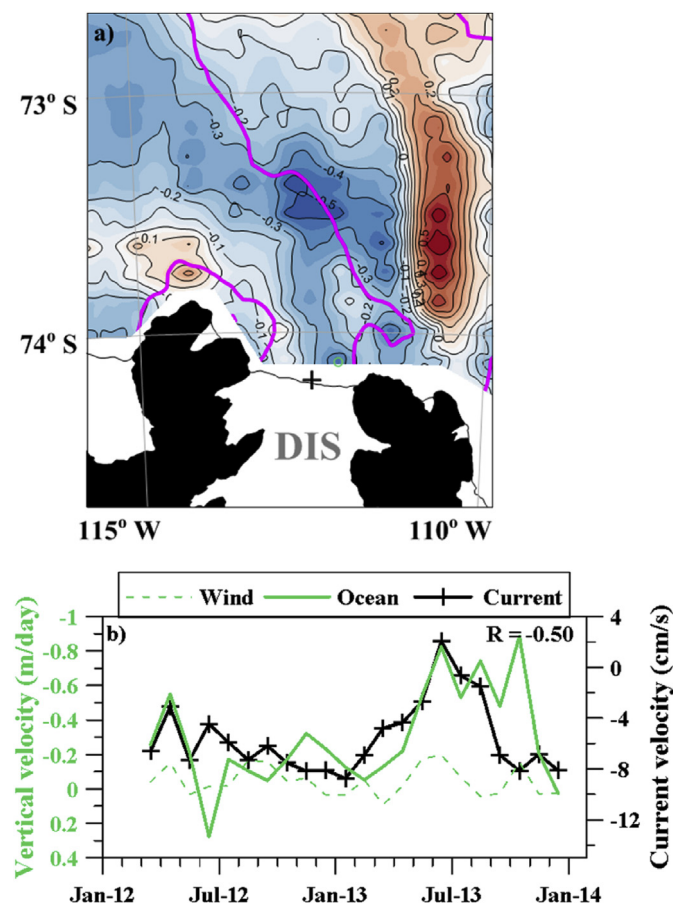


Fig. 9. a) Spatial correlation between monthly averaged coastal current and Ekman vertical velocity. Green circle is the point of maximum correlation and the cross is point of long-term observation of the coastal current. The thick magenta line represents the 500 m isobath. b) Time series of monthly averaged coastal current (crosses and black solid line), Ekman vertical velocity (at the green circle in (a)) calculated by wind stress curl (green dashed line) and by ocean stress curl (green solid line). DIS: Dotson Ice Shelf. (For interpretation of the references to colour in this figure legend, the reader is referred to the web version of this article.)

coastal current and Ekman vertical velocity considering sea ice effects correspond well, except during austral spring (green solid line, $R = -0.50$), but are relatively weakly correlated without considering sea ice effects (green dashed line, $R = -0.34$). For these data sets, the correlation is considered statistically significant when greater than 0.42 (95% confidence interval, $N = 22$). If the negative Ekman vertical velocity increases, the westward coastal current in the near surface layer will decrease because the density distribution descends due to coastal downwelling in the coastal area.

5. Conclusions and summary

The strong westward flow of the AACC, generated by prevailing easterly winds, has been observed in the Dotson Ice Shelf of the Amundsen Sea. This study examined the variability of the baroclinic component of AACC induced by four driving mechanisms: local zonal wind, SIC, thermohaline forcing, and Ekman vertical velocity. The effects of these mechanisms on the seasonal and non-seasonal variabilities of the coastal current around the Dotson Ice Shelf were estimated. The high-frequency variation (<90 days) of the AACC was found to coincide with the short-term density variation. Zonal winds affect the wind-driven component of AACC, and wind-driven downwelling in the coastal area showed negative correlation with the density variation. The coastal downwelling changes of the isopycnoline in front of the Dotson Ice Shelf lead to the eastward flow and weakening of AACC related with the baroclinic effects.

To understand the seasonal variability of the AACC, we compared the westward coastal current with the Ekman vertical velocity using the ocean surface stress, which showed high correlation near the Dotson Ice Shelf. Ekman pumping had a negative feedback on the coastal current in the near surface layer and it changes the isopycnal in front of the Dotson Ice Shelf. These results show that both the seasonal and the short-term variabilities of the AACC are firstly related to the seasonality of salinity variation, based on thermohaline forcing, and secondly to the variability of the isopycnocline, based on Ekman pumping. Therefore, change in the isopycnal distribution is fundamental in explaining the variability of the AACC near the Dotson Ice Shelf.

Acknowledgments

We would like to thank Chang-Su Hong for the acquisition and analysis of the moored station data. We also thank Anna K. Wåhlin for discussion on the mechanisms of the ocean circulation in front of ice shelves. This work was supported by grants (PP15020 and PE15040) from the Korea Polar Research Institute.

References

- Arneborg, L., Wåhlin, A.K., Björk, G., Liljebladh, B., Orsi, A.H., 2012. Persistent inflow of warm water onto the central Amundsen shelf. *Nat. Geosci.* 5 (12), 876–880.
- Assmann, K.M., Jenkins, A., Shoosmith, D.R., Walker, D.P., Jacobs, S.S., Nicholls, K.W., 2013. Variability of circumpolar deep water transport onto the Amundsen Sea continental shelf through a shelf break trough. *J. Geophys. Res. Oceans* 118 (12), 6603–6620.
- Bindoff, N.L., Rosenberg, M.A., Warner, M.J., 2000. On the circulation and water masses over the Antarctic continental slope and rise between 80 and 150 E. *Deep Sea Res. Part II Top. Stud. Oceanogr.* 47 (12), 2299–2326.
- Bindschadler, R., 2006. Hitting the ice sheets where it hurts. *Sci. Wash.* 311 (5768), 1720–1721.
- Carmack, E., Chapman, D.C., 2003. Wind-driven shelf/basin exchange on an Arctic shelf: the joint roles of ice cover extent and shelf-break bathymetry. *Geophys. Res. Lett.* 30 (14), 1778.
- Combes, V., Matano, R.P., 2014. A two-way nested simulation of the oceanic circulation in the Southwestern Atlantic. *J. Geophys. Res. Oceans* 119 (2), 731–756.
- Dutrieux, P., de Rydt, J., Jenkins, A., Holland, P.R., Ha, H.K., Lee, S.H., Schröder, M.,

2014. Strong sensitivity of Pine Island ice-shelf melting to climatic variability. *Science* 343 (6167), 174–178.
- Fahrbach, E., Rohardt, G., Krause, G., 1992. The Antarctic coastal current in the southeastern Weddell Sea. In: *Weddell Sea Ecology*. Springer, Berlin, Heidelberg, pp. 171–182.
- Fennel, W., Johannessen, O.M., 1998. Wind-forced oceanic responses near ice edges revisited. *J. Mar. Syst.* 14 (1), 57–79.
- Ha, H.K., Wählin, A.K., Kim, T.W., Lee, S.H., Lee, J.H., Lee, H.J., Hong, C.S., Arneborg, L., Björk, G., Kalén, O., 2014. Circulation and modification of warm deep water on the central Amundsen Shelf. *J. Phys. Oceanogr.* 44 (5), 1493–1501.
- Häkkinen, S., 1986. Coupled ice–ocean dynamics in the marginal ice zones: upwelling/downwelling and eddy generation. *J. Geophys. Res. Oceans* 91 (C1), 819–832 (1978–2012).
- Hellmer, H.H., Kauker, F., Timmermann, R., Determann, J., Rae, J., 2012. Twenty-first-century warming of a large Antarctic ice-shelf cavity by a redirected coastal current. *Nature* 485 (7397), 225–228.
- Heywood, K.J., Locarnini, R.A., Frew, R.D., Dennis, P.F., King, B.A., 1998. Transport and water masses of the Antarctic slope front system in the eastern Weddell Sea. *Ocean Ice Atmos. Interact. A. T. Antarct. Cont. Margin* 203–214.
- Heywood, K.J., Naveira Garabato, A.C., Stevens, D.P., Muench, R.D., 2004. On the fate of the Antarctic slope front and the origin of the Weddell front. *J. Geophys. Res. Oceans* 109 (C6).
- Jacobs, S.S., 1991. On the nature and significance of the Antarctic slope front. *Mar. Chem.* 35 (1), 9–24.
- Jacobs, S.S., Jenkins, A., Giulivi, C.F., Dutrieux, P., 2011. Stronger ocean circulation and increased melting under Pine Island Glacier ice shelf. *Nat. Geosci.* 4 (8), 519–523.
- Jacobs, S., Jenkins, A., Hellmer, H., Giulivi, C., Nitsche, F., Huber, B., Guerrero, R., 2012. The Amundsen Sea and the Antarctic ice sheet. *Oceanography* 25 (3), 154–163.
- Jenkins, A., Dutrieux, P., Jacobs, S.S., McPhail, S.D., Perrett, J.R., Webb, A.T., White, D., 2010. Observations beneath Pine Island Glacier in West Antarctica and implications for its retreat. *Nat. Geosci.* 3 (7), 468–472.
- Joughin, I., Smith, B.E., Holland, D.M., 2010. Sensitivity of 21st century sea level to ocean-induced thinning of Pine Island Glacier, Antarctica. *Geophys. Res. Lett.* 37 (20).
- Koentopp, M., Eisen, O., Kottmeier, C., Padman, L., Lemke, P., 2005. Influence of tides on sea ice in the Weddell Sea: investigations with a high-resolution dynamic-thermodynamic sea ice model. *J. Geophys. Res. Oceans* 110 (C2).
- Large, W.G., Pond, S., 1981. Open ocean momentum flux measurements in moderate to strong winds. *J. Phys. Oceanogr.* 11 (3), 324–336.
- Lu, P., Li, Z., Cheng, B., Leppäranta, M., 2011. A parameterization of the ice-ocean drag coefficient. *J. Geophys. Res. Oceans* 116 (C7) (1978–2012).
- Lüpkes, C., Birnbaum, G., 2005. Surface drag in the Arctic marginal sea-ice zone: a comparison of different parameterisation concepts. *Boundary-Layer Meteorol.* 117 (2), 179–211.
- Mathiot, P., Goosse, H., Fichet, T., Barnier, B., Gallée, H., 2011. Modelling the seasonal variability of the Antarctic Slope Current. *Ocean Sci.* 7 (4), 445–532.
- Nakayama, Y., Schröder, M., Hellmer, H.H., 2013. From circumpolar deep water to the glacial meltwater plume on the eastern Amundsen Shelf. *Deep Sea Res. Part I Oceanogr. Res. Pap.* 77, 50–62.
- Nakayama, Y., Timmermann, R., Rodehacke, C.B., Schröder, M., Hellmer, H.H., 2014. Modeling the spreading of glacial meltwater from the Amundsen and Bellinghausen Seas. *Geophys. Res. Lett.* 41 (22), 7942–7949.
- Núñez-Riboni, I., Fahrbach, E., 2009. Seasonal variability of the Antarctic Coastal Current and its driving mechanisms in the Weddell Sea. *Deep Sea Res. Part I Oceanogr. Res. Pap.* 56 (11), 1927–1941.
- Orsi, A.H., Whitworth, T., Nowlin, W.D., 1995. On the meridional extent and fronts of the Antarctic Circumpolar Current. *Deep Sea Res. Part I Oceanogr. Res. Pap.* 42 (5), 641–673.
- Padman, L., Fricker, H.A., Coleman, R., Howard, S., Erofeeva, L., 2002. A new tide model for the Antarctic ice shelves and seas. *Ann. Glaciol.* 34 (1), 247–254.
- Pritchard, H.D., Vaughan, D.G., 2007. Widespread acceleration of tidewater glaciers on the Antarctic Peninsula. *J. Geophys. Res. Earth Surf.* 112 (F3) (2003–2012).
- Randall-Goodwin, E., Meredith, M.P., Jenkins, A., Yager, P.L., Sherrell, R.M., Abrahamsen, E.P., Guerrero, R., Yuan, X., Mortlock, R.A., Gavahan, K., Alderkamp, A.-C., Ducklow, H., Robertson, R., Stammerjohn, S.E., 2015. Freshwater distributions and water mass structure in the Amundsen Sea Polynya region, Antarctica. *Elem. Sci. Anthropocene* 3 (1), 000065.
- Rignot, E., Bamber, J.L., van den Broeke, M.R., Davis, C., Li, Y., van de Berg, W.J., van Meijgaard, E., 2008. Recent Antarctic ice mass loss from radar interferometry and regional climate modelling. *Nat. Geosci.* 1 (2), 106–110.
- Scambos, T.A., Bohlander, J.A., Shuman, C.U., Skvarca, P., 2004. Glacier acceleration and thinning after ice shelf collapse in the Larsen B embayment, Antarctica. *Geophys. Res. Lett.* 31 (18).
- Schulze, L.M., Pickart, R.S., 2012. Seasonal variation of upwelling in the Alaskan Beaufort Sea: impact of sea ice cover. *J. Geophys. Res. Oceans* 117 (C6).
- Sverdrup, H.U., 1953. The currents off the coast of Queen Maud Land. *Norsk Geografisk Tidsskrift-Norwegian J. Geogr.* 14 (1–4), 239–249.
- Talley, L.D., Pickard, G.L., Emery, W.J., Swift, J.H., 2011. *Descriptive Physical Oceanography: an Introduction*. Academic press, Elsevier, 555 pp.
- Tchernia, P., 1981. Observation of the Antarctic east wind drift current by using tabular icebergs tracked by satellite. *Antarct. J. U. S.* 15, 83.
- Tchernia, P., Jeannin, P.F., 1980. Observations on the Antarctic East Wind Drift using tabular icebergs tracked by satellite Nimbus F (1975–1977). *Deep Sea Res. Part A. Oceanogr. Res. Pap.* 27 (6), 467–474.
- Thurnherr, A.M., 2010. A practical assessment of the errors associated with full-depth LADCP profiles obtained using Teledyne RDI Workhorse acoustic Doppler current profilers. *J. Atmos. Ocean. Technol.* 27 (7), 1215–1227.
- Tschudi, M., Fowler, C., Maslanik, J., Stewart, J.S., Meier, W., 2016. Polar Pathfinder Daily 25 km EASE-grid Sea Ice Motion Vectors. Version 3. National Snow and Ice Data Center, Boulder, Colorado USA. <http://dx.doi.org/10.5067/057VAIT2AYYY>.
- Walker, D.P., Brandon, M.A., Jenkins, A., Allen, J.T., Dowdeswell, J.A., Evans, J., 2007. Oceanic heat transport onto the Amundsen Sea shelf through a submarine glacial trough. *Geophys. Res. Lett.* 34 (2).
- Wählin, A.K., Yuan, X., Björk, G., Nohr, C., 2010. Inflow of warm circumpolar deep water in the central Amundsen shelf. *J. Phys. Oceanogr.* 40 (6), 1427–1434.
- Whitworth, T., Orsi, A.H., Kim, S.J., Nowlin, W.D., Locarnini, R.A., 1998. Water masses and mixing near the Antarctic slope front. *Ocean Ice Atmos. Interact. A. T. Antarct. Cont. Margin* 1–27.
- Yang, J., 2006. The seasonal variability of the Arctic Ocean Ekman transport and its role in the mixed layer heat and salt fluxes. *J. Clim.* 19 (20), 5366–5387.